

Pulsar Signal: Prediction of Timing Noise and Correction of Atmospheric Delay

Summary

Pulsars, “lighthouses of the universe”, emit a steady stream of highly regular electromagnetic waves. They are considered to be the most accurate clocks in the universe. The observation of its signal has become an important topic. In particular, the prediction of its timing noise and the correction of atmospheric delays. To address these two issues, we fit a specific pulsar timing noise and study the delay times produced by atmospheric refraction at different elevation angles.

We build several models: **Model I: TVF-EMD Model**; **Model II: BDSK-SA Model**, etc.

For Model I, we combine the **EMD** method with a **time-varying filter (TVF)**. For the given pulsar-specific timing noise, we decompose it into five sinusoidal-like intrinsic modal functions (**IMFs**) by the EMD method. In order to solve the modal mixing problem of the IMFs, we introduced the TVF in the EMD iteration process and filtered each IMF to obtain frequency independent IMFs.

- For Task 1, we determined the remaining parameters of the IMFs and summed them to find the functional model S, which fit the original data with **98.61%**.
- For Task 2, we used the derived functional model S to predict the timing noise after a given time period. It is found that in the short term (one month), **the noise decreases and then increases**; in the long term (twenty years), **the noise shows periodic changes with a period of about five years**.

For Model II, we divided the atmosphere into the neutral layer and the ionosphere, and the neutral layer was subdivided into the static atmosphere and the wet atmosphere. For the neutral layer, we used the SA Model to calculate the delay time. And for the ionosphere, we introduced the BDSK Model and determined the parameters in it using the Chapman Model. Combining the above models, we established the BDSK-SA Model.

- For Task 3, we calculated the atmospheric refraction delay of 20G Hz EM waves to be between **7.5 and 7.6 ns** at high elevation angles.
- For Task 4, we calculated an atmospheric refraction delay of **17.4043 ns** at low elevation angles (10°), and the delay is stable up to 10° .

Finally, we performed stability analysis on the SA Model and the BDSK-SA Model. Six cities were selected for the high elevation angle part and their delay errors were **2.48%**. The stability analysis of the latitude parameter was performed at low elevation angles, and the error was **0.65%**. This proves that our model is **stable**.

Keywords: Pulsar, EMD Model, SA Model, Atmospheric Refraction Delay, Timing Noise

Contents

1. Introduction	3
1.1 Background	3
1.2 Restatement	3
1.3 Our Work	4
2. Assumptions and Notations	4
2.1 Assumptions and Justifications	5
2.2 Notations	5
3. Model I : TVF-EMD Model	6
3.1 Model Preparation	6
3.2 Model Building	7
3.2.1 EMD Model	7
3.2.2 Introduction of Time-Varying Filters	8
3.3 Problem Solving	10
3.3.1 Task 1 : Pulsar Timing Noise Fitting	11
3.3.2 Task 2 : Prediction of Pulsar Timing for a Certain Period of Time	12
4. Model II : SA Model	14
4.1 Neutral Atmosphere Refraction Delay	14
4.2 Zenith Delay and Mapping Functions	15
4.3 Resolution of Task 3	16
4.3.1 Numerical Solution	16
4.3.2 Data Collection	17
5. Model III : BDSK-SA Model	18
5.1 Model Preparation	18
5.1.1 Introduction of Ionospheric Delays	18
5.2 Model Building	19
5.2.1 BDSK Model	19
5.2.2 Parameter Fitting	20
5.3 Task 4 : Atmospheric Delay for Observations with Small Elevation Angles	22
6. Sensitivity Analysis	22
7. Strengths and Weakness	24
7.1 Strengths	24
7.2 Weakness	24
8. Conclusion	24
References	25

1. Introduction

1.1 Background

Pulsars are the products of the late evolution of massive stars formed by the collapse of the core, which have important applications in astrophysics, particle physics and satellite navigation. Because pulsars are not affected by the environment and do not tremble with age, they are more stable than any clock on Earth. They are natural timers in vacuum. The pulsar's pulse comes from its rotation, which have been found very stable by actual observations, especially the long-term rotation stability of millisecond pulsars is even better than the performance of the International atomic clock group now in use ^[1]. Therefore, pulsar timing observations can accurately measure pulsar rotation parameters and astrometry parameters.

At present, due to the imperfect timing model and the presence of some sources of error that could not be eliminated, the further improvement of the accuracy of pulsar timing analysis is limited, which is mainly reflected in the fluctuation of pulsar timing residual. In addition, the main consideration of pulsar time, pulse Arrival time (TOA), is also affected by various delay effects, including the attenuation of the atmospheric time signal.

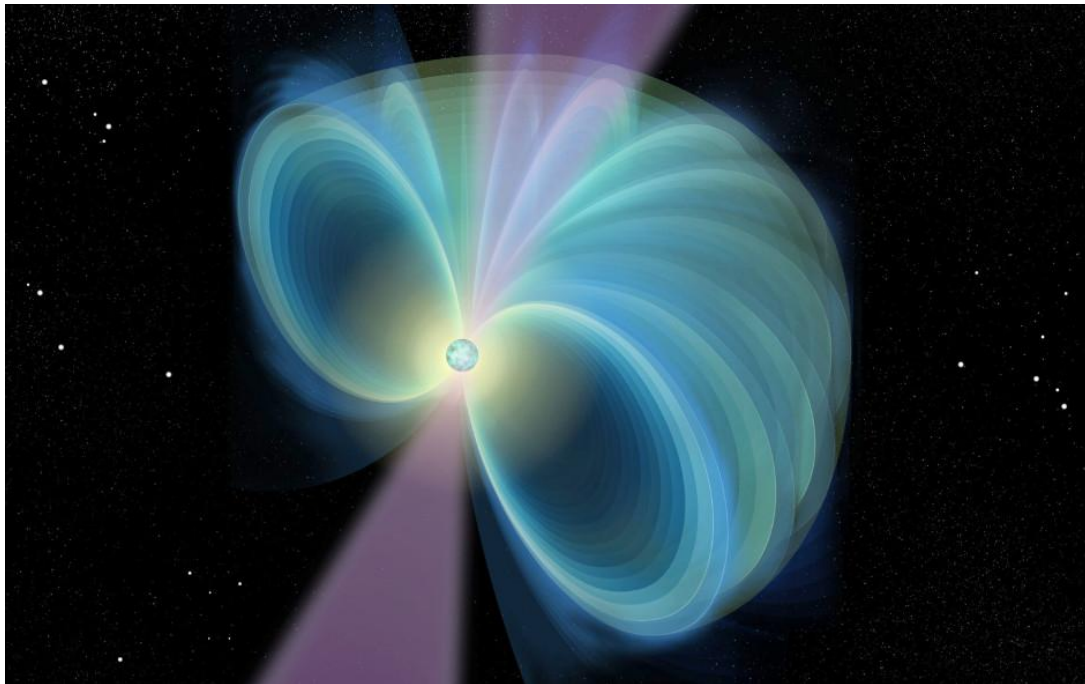


Figure 1: A Pulsar Image^[2]

1.2 Restatement

Considering the background information and limiting conditions identified in the problem statement, we are supposed to address the following issues:

- Build a model to simulate the pulsar timing noise in the problem statement.
- Make short-term and long-term forecasts on the future trend of the pulsar noise in

- the problem statement.
- Modeling the refractive time delay for radio observation frequencies above 20 GHz.
 - Modeling the atmospheric time delay for for observations with small elevation angles (10 degrees or less).

1.3 Our Work

Our solution mindmap is shown below.

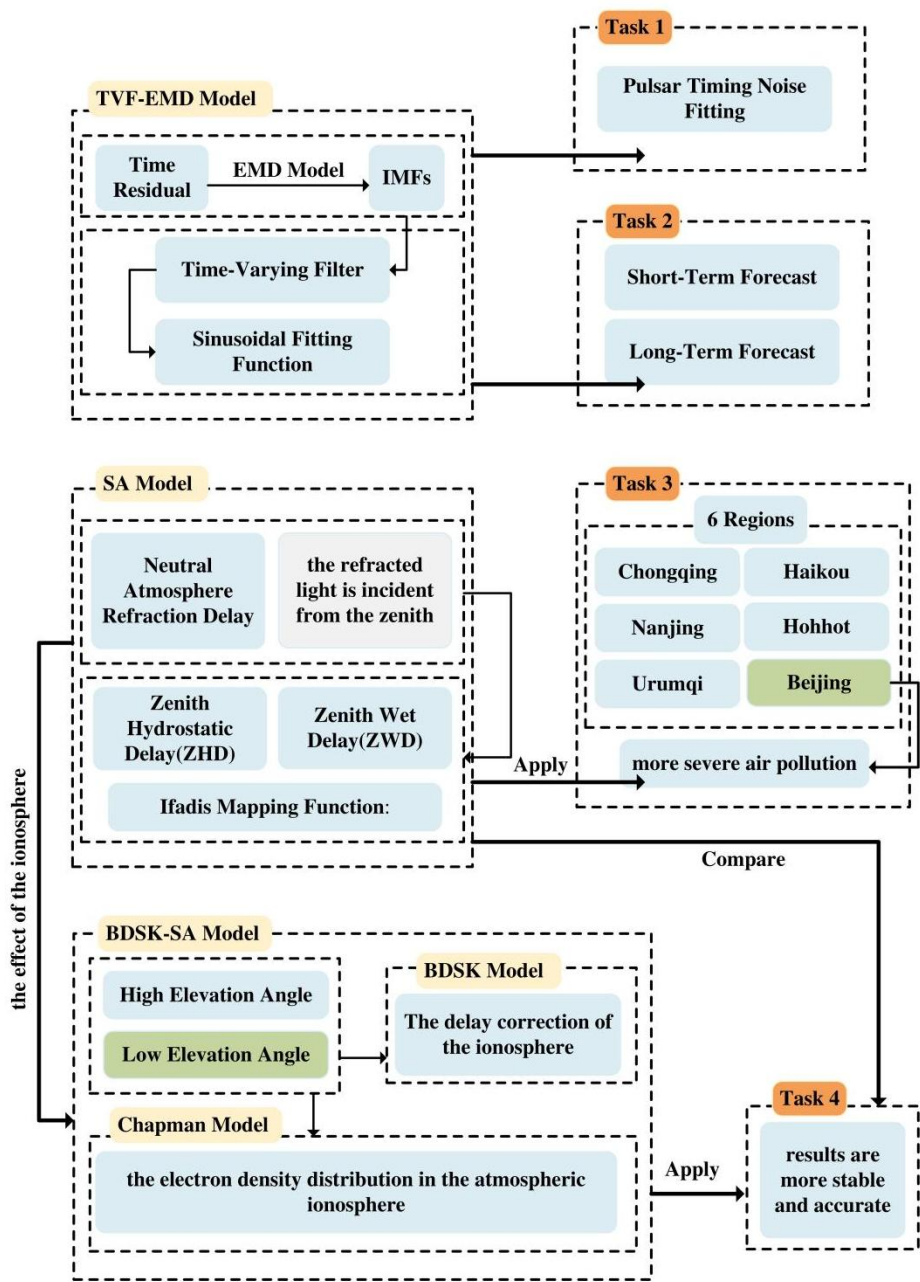


Figure 2: Our Work

2. Assumptions and Notations

2.1 Assumptions and Justifications

- **Assumption 1: Different factors produce pulsar timing noise at different frequencies.**

Justification 1: Many factors in the universe can lead to the production of timing noise, such as stardust impurities, gravitational waves, or other pulsars from similar positions. Due to their different production principles, the signal waveforms of the noise can vary quite a bit, and the proposed synthesized trigonometric functions have different frequencies, amplitudes, and other characteristics.

- **Assumption 2: The weather does not change significantly when the timing noise is received.**

Justification 2: When receiving the timing noise signal, we assume that the weather is smooth and that the raw data is not affected by sudden changes in the weather, in order to allow us to derive an adaptive function and predict the next data.

- **Assumption 3: Solar radiation is homogeneous, ignoring the scattering effect of solar radiation in the atmosphere.**

Justification 3: In optics we refer to sunlight as parallel light, due to the fact that the distance between the Sun and the Earth is so great that it far exceeds the diameter of the sun. Here we use the same assumption, ignoring angular differences in radiation, that solar radiation is the same at all locations at equal heights in the atmosphere.

- **Assumption 4: The change in electron density in the ionosphere is determined only by the photoionization and complexation processes.**

Justification 4: The molecules and atoms of the Earth's upper atmosphere are ionized by solar ultraviolet, X-rays and energetic particles, producing free electrons and positive and negative ions. But here we consider only the effect of sunlight.

2.2 Notations

Table 1: Notations Table

Notations	Definition
$S_{Original}$	Original data
S_{Fitted}	The fitted function
IMF_i	The eigenmode function
E	Error of the fitted curve to the original curve
R	The accuracy of the fit
L	Optical length
ΔL	Atmospheric refraction delay

z	The incidence angle of the electromagnetic waves
r	Centre distance
Φ	The latitude of the observation station
ZHD	Zenith Static mechanics delay
ZWD	Zenith wet delay
MFh	Static mapping function
MFw	Wet mapping function
MFf	Ionosphere mapping function
t_n	The neutral atmosphere refraction delay time
I	The ionosphere refraction delay time
t_{total}	Total atmospheric delay

3. Model I : TVF-EMD Model

3.1 Model Preparation

Due to the variety of sources of pulsar timing delay, the physical mechanism is complex, involving a series of relative theory^[3] and perturbation theory, which has a certain randomness. When the pulse signal passes through the interstellar medium during propagation (such as changes in electron density), the propagation speed of the signal will change, resulting in time delay. In particular, when pulsar signals propagate in the interstellar medium, the uneven distribution of electron density causes the signals to undergo different propagation paths, resulting in delays^[4].

The density of electrons in the atmosphere affects the speed of electromagnetic wave propagation, especially in the ionosphere. As the pulsar signal passes through the Earth's atmosphere, the inhomogeneity of the ionosphere leads to variations in propagation speed, which causes a delay in the signal. As a result, the difference between the predicted pulse arrival time (PT) and the actual arrival time (PT-TT) is very random, and no generalized formula has been found that can be accurately fitted to the combined recursion, which brings great challenges to our forecasting efforts.

Observing the PT-TT image in the problem, it can be found that it has 5 peaks almost equally spaced, with little difference in value. In addition, there are 1 to 3 extreme values between the peaks, and the data are evenly distributed above and below the x-axis. Therefore, it can be approximated as a quasi-periodic function. Fit it with a superposition of trigonometric functions of different periods and add a correction term for the residuals at the end to make a better fit to the original data.

$$S_{Original}(t) = \sum_{i=1}^n a_i \sin(\omega_i t + \varphi_i) + \sigma(t) \quad (1)$$

3.2 Model Building

3.2.1 EMD Model

To decompose $S(t)$, we develop the **EMD Model**. The EMD method is an efficient tool for decomposing a signal sequence, which decomposes a time series into a finite number of intrinsic modal function (IMF) components and a residual trend term $\sigma(t)$ [5]. Our goal is to obtain a series of sinusoidal functions. Based on the properties of the sinusoidal functions, we specify the IMF as follows:

- The number of extreme points of the IMF does not differ from the number of zero points by more than one;
- The extreme values of the IMF have similar absolute values to the extreme values, i.e., the envelope has a mean value of zero;
- There is one and only one extreme value between two neighboring zeros of the IMF;

The following is the implementation of the EMD method:

- First set the original sequence as $S_{Original}(t)$, find out all its local maxima and minima in the given interval, and fit the upper and lower two envelopes $u_1(t)$, $d_1(t)$ with cubic spline interpolation;
- Then find the mean value of the two envelopes, and subtract the mean value from the original series.

$$m_1(t) = \frac{1}{2} [u_1(t) + d_1(t)] \quad (2)$$

$$h_1(t) = S_{Original}(t) - m_1(t) \quad (3)$$

- This gives us a rough IMF, but it does not necessarily satisfy our conditions, so we need to iterate it. Repeat the first two steps with $h_1(t)$ as the new original sequence, assuming that the condition is satisfied after k iterations

$$h_{1k}(t) = h_{1(k-1)}(t) - m_k(t) = IMF_1 \quad (4)$$

This gives us $C1$, our first IMF. It is then subtracted from the original sequence to get the new original sequence S . Repeating steps (1)-(3), S becomes a monotone function $\sigma(t)$.

$$S_{Original}(t) = \sum_{i=1}^n IMF_i + \sigma(t) \quad (5)$$

EMD completed.

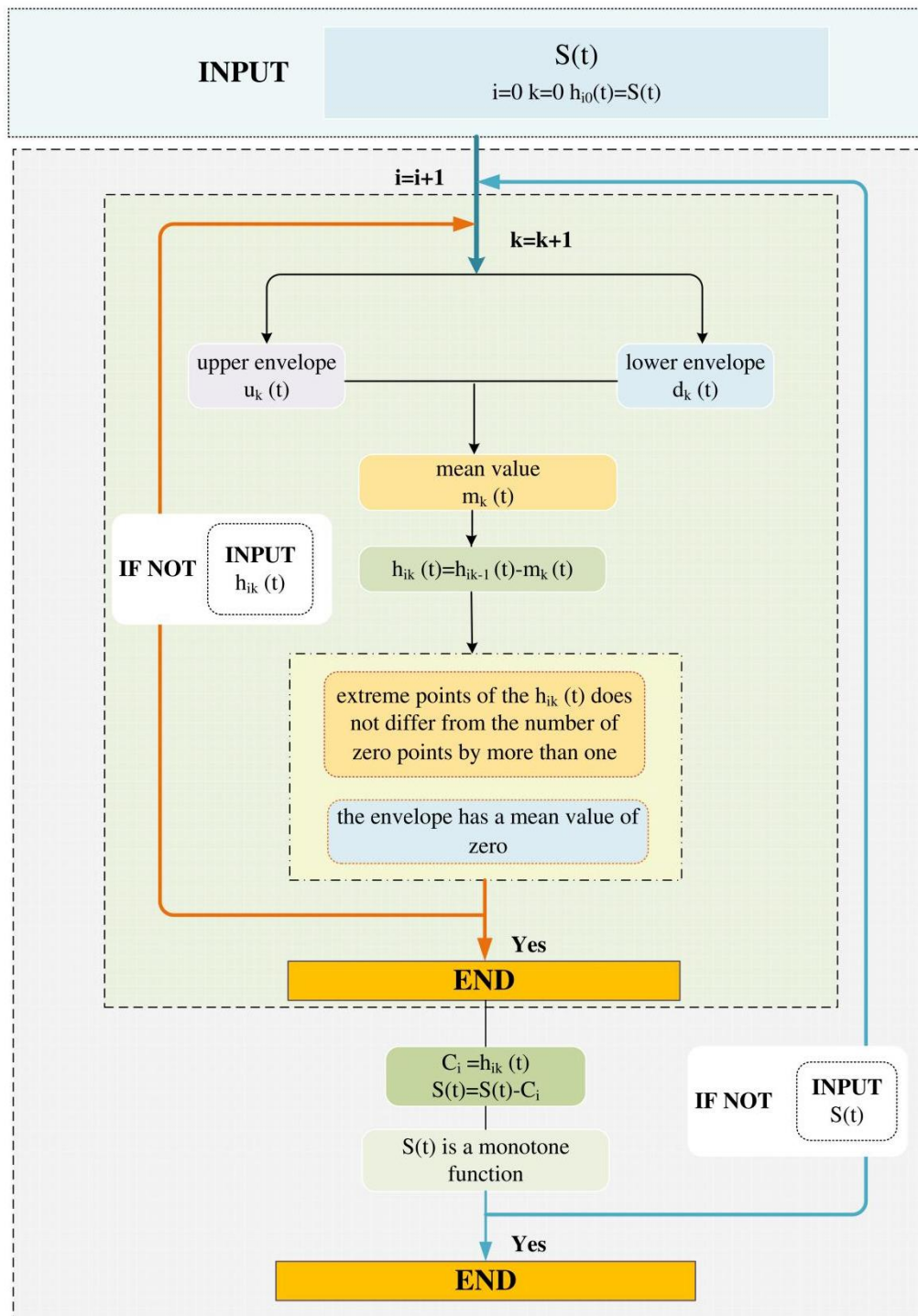


Figure 3: Flowchart of EMD Method

3.2.2 Introduction of Time-Varying Filters

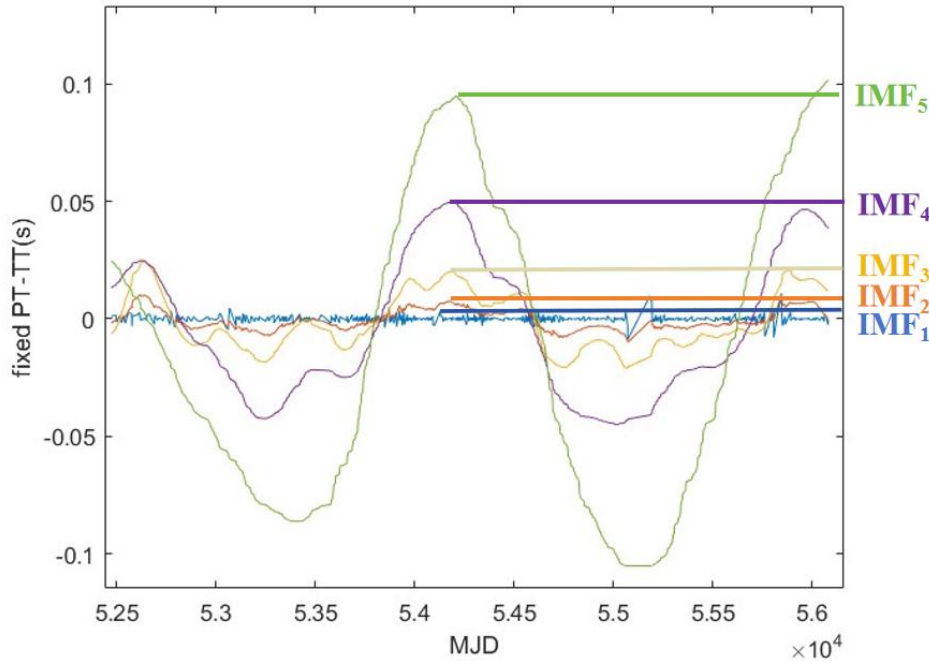


Figure 4: The Decomposed Five IMF

Through EMD, we obtain five IMFs, but these IMFs do not fit the sinusoidal function well, and the traditional EMD method suffers from the **Mode Mixing** and **Intermittency Problems**.

The modal mixing problem refers to the fact that during EMD decomposition, signal components that are supposed to belong to different frequency ranges are incorrectly mixed together, resulting in the decomposed IMFs that do not make physical sense. This kind of mixing usually occurs in parts of the signal where the frequency changes rapidly, or when the different frequency components contained in the signal are too close to each other.

The intermittency problem refers to the fact that during the EMD decomposition process, certain local features in the signal (such as transient changes, abrupt changes or breaks) may lead to distortion in the IMF decomposition. The EMD method may suffer from modal incoherence and unreasonable energy distribution when dealing with signals that contain intermittent features.

The main influence that will affect our results here is modal mixing. We need to decouple the IMFs at different frequencies.

We take the TVF-EMD^[6] method to decouple the IMFs. The specific process is to introduce a time-varying filter to filter each IMF and then output the filtered IMFs. In conventional filters, the transfer function of the filter is time-invariant, i.e., its coefficients do not change with time. For time-varying filters, the coefficients, gain, or frequency response of the filter are adjusted with time. For example, the cutoff frequency of the filter can be set to change over time, or certain parameters of the

filter's transfer function can change over time. This ensures that the model can be dynamically adjusted in a time-dependent manner in the process of solving the IMF, enhancing the adaptivity of the model.

The mathematical description of a time-varying filter is: suppose we have a time-varying filter with an input signal $x(t)$ and an output signal $y(t)$. The behavior of the filter can be described by the convolution operation:

$$y(t) = (h(t) * x(t)) = \int_{-\infty}^{+\infty} h(t - \tau) x(\tau) d\tau \quad (6)$$

$$y[n] = \sum_{k=-\infty}^{\infty} h[n, k] x[k] \quad (7)$$

Where (6) is the continuous case and (7) is the discrete case. $h[n, k]$ is a time-varying impulse response, where n denotes the current moment and k is the index associated with the input signal $x[k]$. According to the related information, we can simplify the time-varying filtering in the TVF-EMD model and we introduce the following filter:

$$y[n] = \frac{x[n] + \eta(y[n+1] + y[n-1])}{1 + 2\eta} \quad (8)$$

Where η is the filter coefficient, the larger η is, the higher the degree of filtering. But it will lead to a higher degree of distortion in the signal.

3.3 Problem Solving

We take $\eta = 0.1$ here and make a separated IMF image, which gives us five images of sine-like functions, and each of the five IMFs has a different period and amplitude.

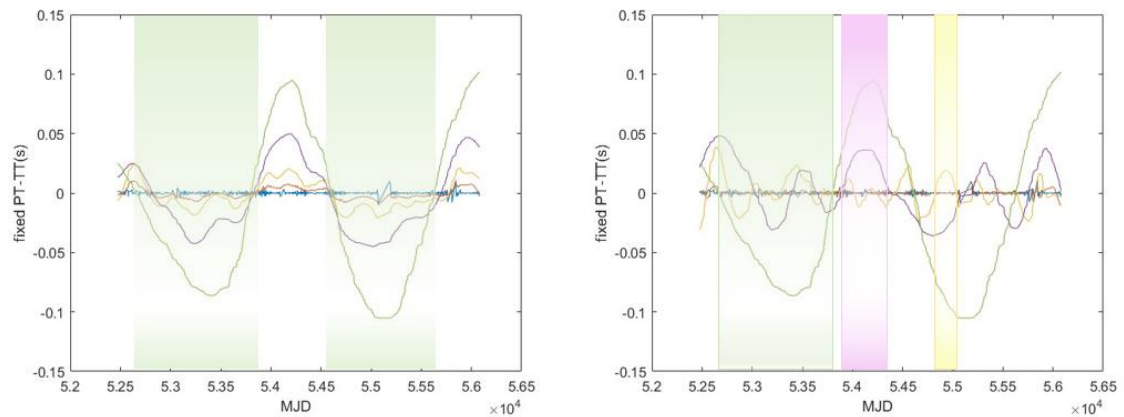


Figure 5: Different Period and Amplitude of the Five IMFs

After obtaining the separated IMF, we can perform trigonometric fitting. The IMF data were imported into Origin software respectively, and then the sine function in waveform function library was utilized for nonlinear fitting

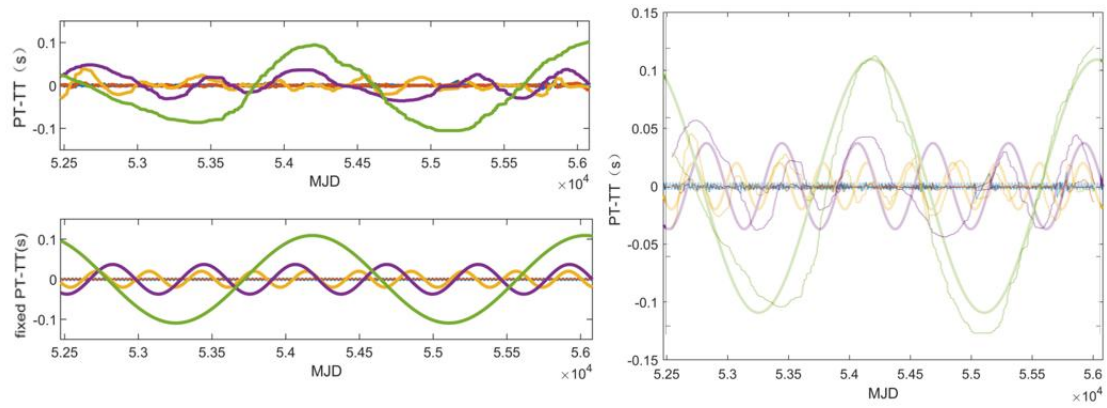


Figure 6: The Five IMF's Plots After the Fit

Let the curve to be found be

$$S_{Fitted}(t) = \sum_{i=1}^5 a_i \sin\left(\frac{t}{t_i} + \varphi_i\right) + d \cdot t \quad (9)$$

The fit gives

Table 2: Parameter Declaration

parameter	identifier	value
a_i	1	0.10933 ± 0.00164
	2	0.0371 ± 0.00768
	3	0.02 ± 0
	4	0.01
	5	0.005
t_i	1	926.16268 ± 0.07567
	2	309.83227 ± 0.35226
	3	177.8 ± 0
	4	$2.24651\text{E-}4 \pm 0.00145$
	5	0.00314 ± 0.00145
φ_i	1	-132
	2	-132
	3	-132
	4	-132
	5	-132
d		0 ± 0

3.3.1 Task 1 : Pulsar Timing Noise Fitting

We then substitute these fitted parameters into equation (9), graph and compare with the original data.

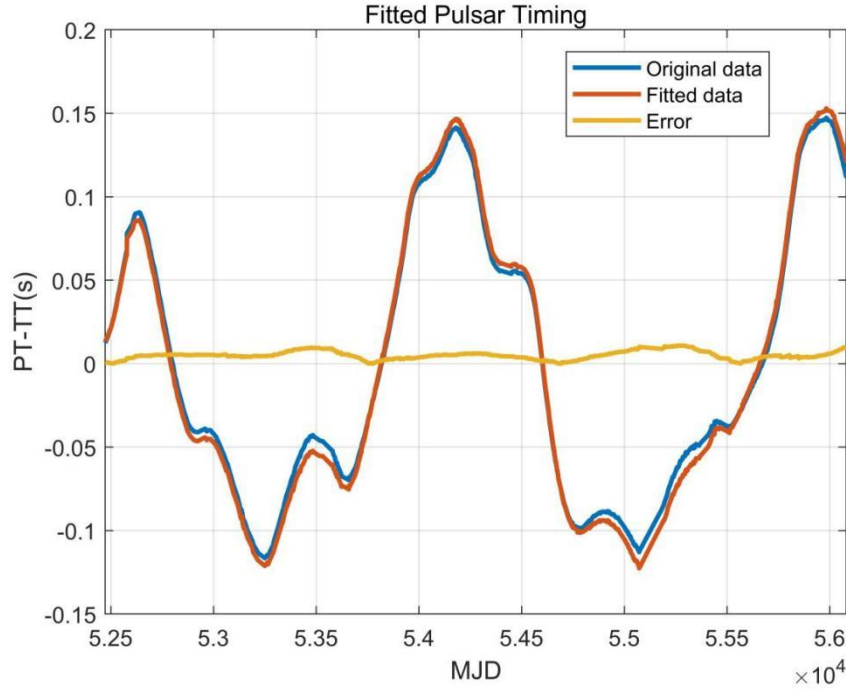


Figure 7: Comparison of Origin Image and Fitted Curve

The above figure shows the absolute value of the original image, the fitted curve and their difference, and it can be noticed that the error is very small. We use the following equation to quantify the accuracy of the fit and define the accuracy as R.

$$R = 1 - E = \left(1 - \sum_{t=t_{start}}^{t_{end}} \left[\frac{|S_{Original}(t) - S_{Fitted}(t)|}{|S_{Original}(t)|} \right]^2 \right) \times 100\% \quad (10)$$

Calculated $R = 98.61\%$, which satisfies the requirement of a fit greater than 95%.

3.3.2 Task 2 : Prediction of Pulsar Timing for a Certain Period of Time

- **Short-term forecast**

First, we fit the 83 data points given in Appendix 1 with our calculated $S(t)$. Using equation (10), which represents the accuracy, we can calculate $R = 97.20\%$, which indicates that the expression calculated with the TVF-EMD model can be applied to this time period. The time given in Appendix 1 was selected and expanded backward in steps of 1 to obtain 30 data points, i.e., predictions from a few days to a month:

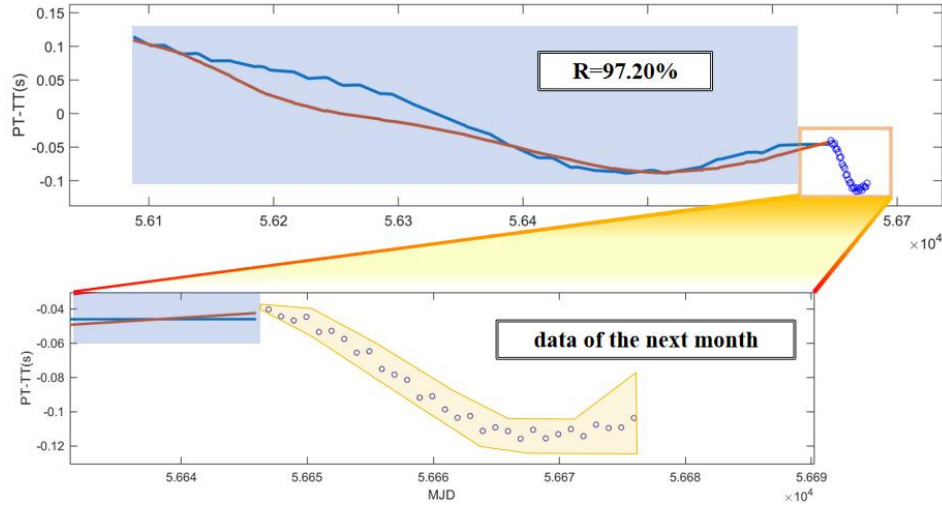


Figure 8: Predictions From a Few Days to a Month

Table 3: Data Points for the Predicted Month

MJD	56647	56648	56649	56650	56651	56652	56653	56654	56655	56656
PT-TT/s	-0.04	-0.04	-0.05	-0.04	-0.05	-0.05	-0.06	-0.07	-0.06	-0.08
	56657	56658	56659	56660	56661	56662	56663	56664	56665	56666
	-0.08	-0.08	-0.09	-0.09	-0.10	-0.10	-0.10	-0.11	-0.11	-0.11
	56668	56669	56670	56671	56672	56673	56674	56675		
	-0.11	-0.12	-0.11	-0.11	-0.11	-0.11	-0.11	-0.10		

The specific coordinates of the data points for the predicted month are shown in the table above. Combining the images, it can be seen from the table that the PT-TT value first decreases and starts to increase after reaching a minimal point near (56668, -0.11).

- **Long-term forecast**

We similarly selected the times from Appendix 1 and expanded them backward with a regular step size of 10 to obtain 800 data points. Using our computed $S(t)$, we draw an image with this time series as the horizontal coordinate, which allows us to predict the change in pulsar timing noise for the next nearly two decades:

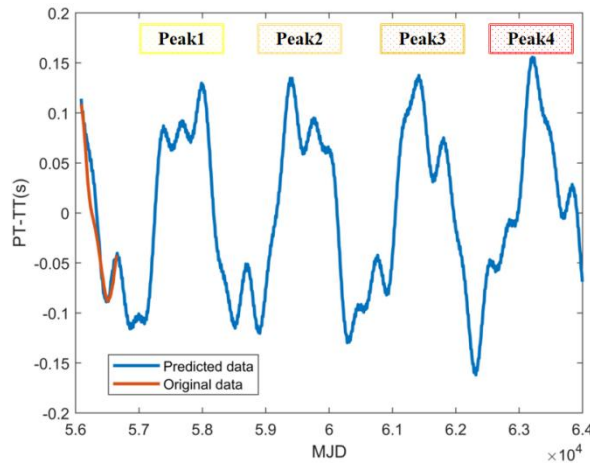


Figure 9: Long-term Prediction of Pulsar-timing Noise

As can be seen from the image, the variation of the pulsar timing noise is a quasi-periodic function with extremes between the two peaks. It is similar to the data image given in the problem statement. It is expected that the pulsar timing noise varies approximately periodically over the next twenty years, with four peaks, i.e., four cycles. Each cycle is about five years.

The periodic variation of pulsar timing noise provides us with important astrophysical and cosmological information. For example, it can reveal the effect of the environment in which the pulsar is located (e.g., the distribution of matter, the structure of the magnetic field, the non-uniformity of the interstellar medium, etc.) on the timing signal. In addition, the timing noise of pulsars is closely related to the distribution and motion of matter in the Milky Way, so long-term monitoring of pulsar signals may reveal more detailed information about the structure of the Milky Way, the distribution of the interstellar medium, and even the gravitational influence of other galaxies. By monitoring the timing data of these pulsars and exploiting the periodic variations in the pulsar timing noise, scientists are able to identify and analyze low-frequency gravitational wave sources, especially from supermassive black hole mergers, gravitational wave backgrounds from primordial cosmic times, and so on.

4. Model II : SA Model

4.1 Neutral Atmosphere Refraction Delay

The neutral atmosphere is a synthesis of the troposphere, stratosphere, mesosphere or part of the thermosphere, and is the layer of the atmosphere from the earth's surface to an altitude of about 60-80 km. In the medium space of the neutral atmosphere, signal propagation follows Fermat's law, i.e., the signal propagates at any two points P_1 and P_2 in space by taking the shortest distance and the propagation time by taking the minimum value. Or the optical length of an actual ray of light between any two points P_1 and P_2 is shorter than the optical length of any other curve connecting these two points. The optical length is defined as

$$L = \int_{P_1}^{P_2} n dl = c \int_{P_1}^{P_2} dt \quad (11)$$

where n , dl are the group refractive index and line element on the signal propagation path, respectively, and c is the propagation speed of electromagnetic wave in vacuum. The optical length L is the direct result of the distance measurement between points P_1 and P_2 by electromagnetic method, and the optical path of the signal is also called the a geodesic. The atmospheric refractive delay of the signal is the difference between the optical distance between points P_1 and P_2 and their geometrical straight-line distance, i.e.

$$\Delta L = \int n dl - \int dX = \int_{R_g} (n-1) dl + \left(\int_{R_g} dl - \int_X dX \right) = \Delta L_1 + \delta L \quad (12)$$

Since $(n-1)$ is too small, we define $N = (n-1) \times 10^6$.

where ΔL_1 is the main term of the neutral atmospheric refraction delay. The second term δL at the right end of Eq. (12) is the light (ray) bending correction in the atmospheric refraction delay.

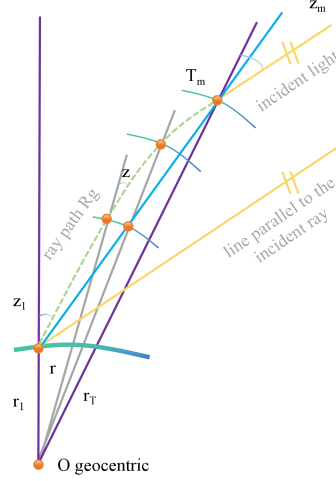


Figure 10: The Schematic Diagram of the Refraction Delay

The schematic diagram of the refraction delay in the neutral atmosphere is shown in Fig. 10. Under the assumption of a spherically symmetric atmospheric model, it is assumed that the electromagnetic wave passes through the point T_m at the top of the neutral atmosphere and follows the path R_g to the station P_1 . The angle of incidence of the electromagnetic wave at point T_m is z_m , and the angle of incidence at station P_1 is z_1 (depending on the zenith distance). The geocentric distance of station P_1 is r_1 , and the geocentric distance of point T_m is r_T ; the angle of incidence of the electromagnetic wave at any point on the propagation path is z , and the geocentric distance is r . According to the Burger's formula for electromagnetic wave propagation, and the geometric relationship at the time of incidence, we have:

$$nr \sin z = n_1 r_1 \sin z_1 \quad (13)$$

$$dr = dl \sin E = dl \cos z \quad (14)$$

Eventually we can get:

$$\Delta L_1 = 10^{-6} \times \int_r^{r_T} \frac{Nnr}{\sqrt{n^2 r^2 - (n_1 r_1 \sin z_1)^2}} dr \quad (15)$$

4.2 Zenith Delay and Mapping Functions

If the refracted light is incident from the zenith, we have $z_1 = 0$ and the original equation becomes:

$$\Delta L_1 = 10^{-6} \times \int_r^{r_T} N dr = 10^{-6} \times \int_r^{r_T} (N_d + N_w) dr = ZHD + ZWD \quad (16)$$

where N_d and N_w are the refractive index differences due to static atmosphere and

water vapor, respectively. The zenith delays produced by them are called zenith static delay or zenith hydrostatic delay (ZHD), and zenith wet delay (ZWD), respectively. Often, the mapping functions of the two are additionally taken into account:

$$\Delta L(E) = ZHD \times MF_h(E) + ZWD \times MF_w(E) \quad (17)$$

$MF_h(E)$, $MF_w(E)$ are called hydrostatic mapping function and wet mapping function respectively. There are different types of mapping functions, here we use the **Ifadis mapping function**:

$$MF(E) = \frac{1 + \frac{a}{b}}{1 + \frac{c}{\sin(E) + \frac{a}{\sin(E) + \frac{b}{\sin(E) + c}}}} \quad (18)$$

For static and wet atmospheres, a, b, c have different values (complete the values of a, b, c).

4.3 Resolution of Task 3

4.3.1 Numerical Solution

Some of the basic parameters of the Earth are shown in the table:

Table 4: Parameter Declaration

Parameters	Displayed Formula	Parameters	Displayed Formula
C_1	α	p_w	$H_{rel}(\frac{T_0}{247.1})^\delta$
C_2	gM_d / S	g	$9.784 \times (1 - 26 \times 10^{-4} \cos 2\Phi - 28 \times 10^{-8} h_0)$
C_3	$C_2 / C_1 = \gamma$	A	$(287.604 + \frac{1.6288}{\lambda^2} + \frac{0.0136}{\lambda^4}) \times \frac{273.15}{1013.25} \times 10^{-\epsilon}$
C_4	δ	C_7	$\frac{A(C_5 + 11.2684 \times 10^{-6} p_w)}{T_0}$
C_5	$\frac{p_w(1 - M_d / M_w)\gamma}{\delta - \gamma}$	C_8	$\frac{\alpha(\gamma - 1)C_6}{T_0}$
C_6	$\frac{A(p + C_5)}{T_0}$	C_9	$\frac{\alpha(\delta - 1)C_7}{T_0}$

The atmospheric index N_d in the troposphere, i.e. the wet atmosphere, can be

expressed as $N_d = (n_d - 1) \times 10^6$.

$$n_d = 1 + [C_6 \left(\frac{T}{T_0}\right)^{\gamma-2} - C_7 \left(\frac{T}{T_0}\right)^{\gamma-2}] \quad (19)$$

$$T = T_0 - \alpha(r - r_0)$$

In the stratosphere, also known as the static atmosphere, the atmospheric index NW can be expressed as $N_w = (n_w - 1) \times 10^6$.

$$T = T_0 - \alpha(r_t - r_0) \quad (20)$$

$$n_w = 1 + (n_t - 1)e^{-C_2(r - r_t)/T_t}$$

where $r_t = R_E + h_t$.

$$\Delta L_1 = 10^{-6} \times \int_r^{r_t} N dr = 10^{-6} \times \int_r^{r_t} (N_d + N_w) dr = ZHD + ZWD \quad (21)$$

$$\Delta L(E) = ZHD \times MFh(E) + ZWD \times MFw(E)$$

Finally, according to this formula, we can calculate:

$$t = \Delta L / c \quad (22)$$

4.3.2 Data Collection

We collected basic meteorological data for a total of six regions at the National Weather Data Center:



Figure 11: The Location of the Six Regions

Table 5: Data of the Six Regions

Region/Data	Temperatures (°C)	Pressure (hPa)	Relative Humidity(%)	Observatory Height(m)	Latitude of the Observatory
Chongqing	16	1019	84%	394	29°32'
Urumqi	4	1037	49%	920	42°45'
Beijing	14	1030	32%	43.5	39°26'
Nanjing	20	1020	98%	27.9	31°20'
Hohhot	-3	1038	37%	1040	40°51'
Haikou	28	1012	85%	8	19°40'

Calculating the atmospheric refraction delay time for these six regions we obtain:

Table 6: the Atmospheric Refraction Delay Time for six Regions

Time/Region	Chongqing	Urumqi	Beijing	Nanjing	Hohhot	Haikou
T(ns)	7.6185	7.6744	7.7176	7.6026	7.6857	7.5367

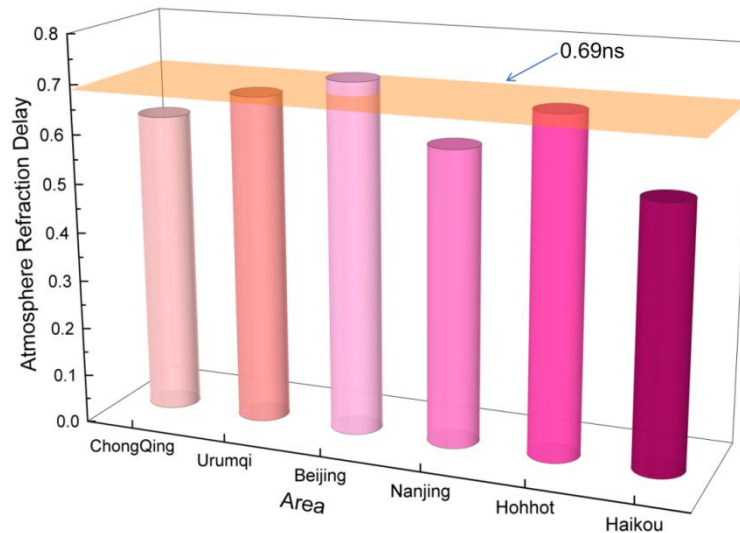


Figure 12: The Atmospheric Refraction Delay Time

The atmospheric delay refraction time of the six regions is only slightly larger than 7.69 ns in Beijing, which we believe is due to the more severe air pollution in Beijing on that day, which affects the measurement of the atmospheric delay data.

5. Model III : BDSK-SA Model

5.1 Model Preparation

5.1.1 Introduction of Ionospheric Delays

In Task 3, we develop the Saastamoinen Model (SA) incorporating the Ifadis mapping function to study the atmospheric refraction delay at high elevation angles. The height of the elevation angle mainly affects the length of the path of the signal propagating through the atmosphere. At high elevation angles, the signal is close to vertical incidence, travels a shorter distance in the atmosphere, and is less affected by atmospheric refraction in all layers. At low elevation angles, on the other hand, the signal is incident nearly horizontally and travels a much longer distance through the atmosphere, which results in a delay that deviates from that at high elevation angles.

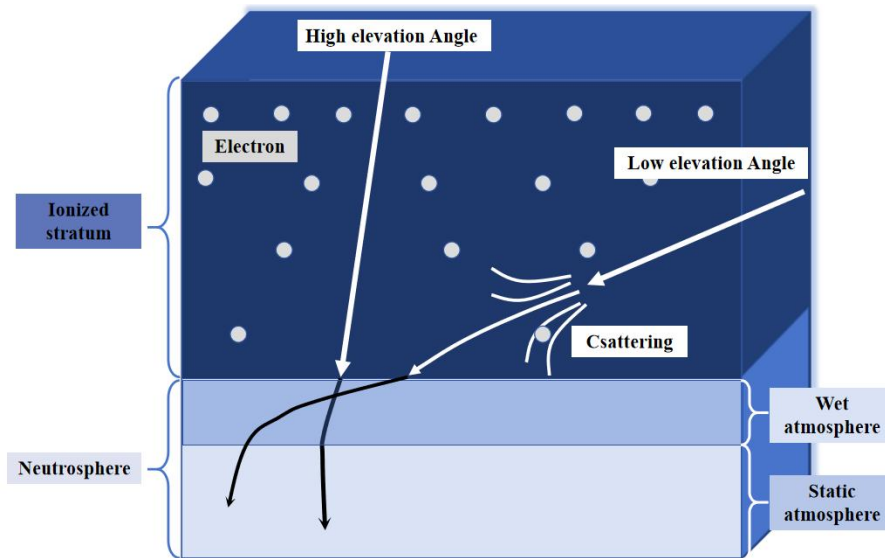


Figure 13: Ionized Stratum and Neutral Layer

As shown in the figure, we can approximate the division of the atmosphere into a neutral layer and an ionosphere. In Task 3, we ignored the effect of the ionosphere because it interferes with the propagation of signals mainly through the scattering of electrons. The scale and mass of electrons and their tiny size and limited density in the atmosphere result in an extremely small probability that an electromagnetic wave will encounter an electron and scatter during propagation.

According to the law of conservation of momentum, the electrons in the atmosphere have almost no effect on the propagation of vertically incident electromagnetic waves, so their scattering of signals at high elevation angles is negligible. However, if the elevation angle does not exceed 10° , the path length of the electromagnetic wave propagation increases dramatically, which leads to a significant increase in the probability of collision with electrons. Thus the effect of the ionosphere is not negligible. So we introduce a correction term for the ionosphere when calculating the atmospheric delay at low elevation angles.

5.2 Model Building

5.2.1 BDSK Model

The ionosphere is a part of the Earth's atmosphere located in the altitude range of about 60 to 1,000 kilometers. It consists of charged particles that affect GPS signals passing through the ionosphere, resulting in slower signal propagation and delays. This delay in the ionosphere is a significant source of error for GPS positioning accuracy. The Klobuchar Model is based on research conducted in the 1970s and is intended to provide a simple but effective method for GPS systems to estimate the delay caused by the ionosphere. The model uses a simple parametric approach with eight coefficients, and ^[7] by combining it with observations of GPS satellite signals, the ionospheric delay can be estimated and corrected accordingly.

By reviewing the literature, we found an improved BDSK model, different from the

traditional Klobuchar model, which is based on the BeiDou Satellite Navigation (BDS) and corrects eight parameters of the original model, which are available on the BDS and updated in real time. The delay correction of the ionosphere based on the BDSK model can be calculated by the following equation [8]:

$$I(t) = \begin{cases} \text{Delay} + A \cos\left[\frac{2\pi(t-50400)}{B}\right], & |t-50400| < \frac{B}{4} \\ \text{Delay}, & |t-50400| \geq \frac{B}{4} \end{cases} \quad (23)$$

where Delay is the nighttime delay constant, usually taken as 5 ns. A is the amplitude of the cosine function, B is the period of the cosine function, and t is the local time at the IPP (Ionospheric Pierce Point).

The formulas for A and B are given below:

$$A = \begin{cases} \sum_{i=1}^4 a_i |\Phi|^2, & A \geq 0 \\ 0, & A < 0 \end{cases} \quad (24)$$

$$B = \begin{cases} 172800, & B \geq 172800 \\ \sum_{i=1}^4 b_i |\Phi|^2, & 72000 \leq B < 172800 \\ 72000, & B < 72000 \end{cases} \quad (25)$$

where a_i and b_i are the 8 parameters of the model. When converting vertical ionospheric delay to apparent ionospheric delay (i.e., tilted ionospheric delay), the mapping function MFf needs to be used as follows:

$$MFf = \frac{1}{\sqrt{1 - \left(\frac{R_E \cos z}{r}\right)^2}} \quad (26)$$

The next computation is the same as the SA model for Task 3, and finally the two delays can be combined

$$t_{total} = t_n + I \quad (27)$$

5.2.2 Parameter Fitting

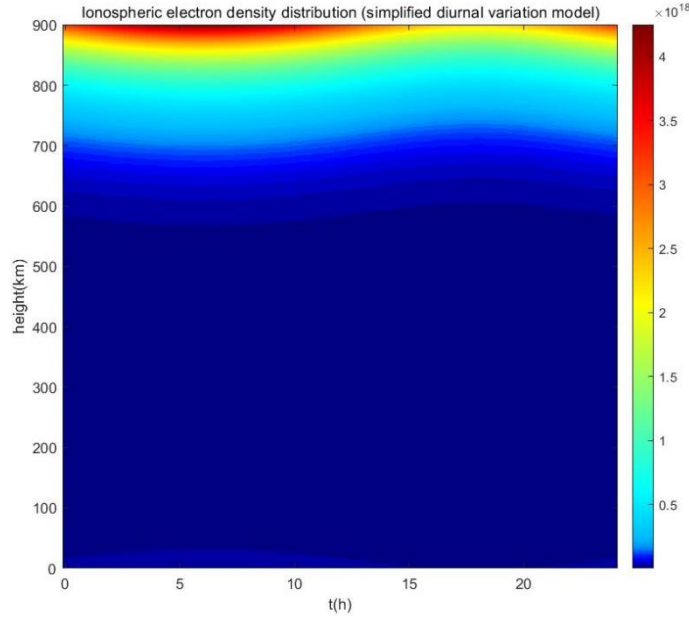


Figure 14: Electron density distribution under the Chapman model

The Chapman Model ^[9] is used to describe the electron density distribution in the atmospheric ionosphere, especially under the influence of photoionization. In order to derive expressions for the Chapman model, we need to consider the following key processes: photoionization and recombination processes, and their effect on electron density with height.

According to our assumptions that the solar radiation is homogeneous, that the absorption of pulsar signals by gas molecules of the atmosphere follows an exponential decay law, and that the variation of the electron density in the ionosphere is determined only by the process of photoionization and compounding, we can write a continuity equation for the electron density:

$$\frac{dN_i(h)}{dh} = \zeta(h) - b_i N(h) = \zeta_0 I_0 \exp(-a_i h) - b_i N(h) \quad (28)$$

where I_0 is the intensity of radiation on the ground. ζ is the photoionization rate, which indicates the rate of generation of electrons per unit height. Solving the differential equation we get N versus a , b .

$$N_i(h) = \frac{\zeta_0 I_0}{b_i - a_i} \exp(-a_i h) [1 - \exp(-b_i h + a_i h)] \quad (29)$$

The data for N can be obtained by looking up the data, picking a specific time period and Taylor expanding equation (29). Using the polynomial obtained, a polynomial fit is performed in Origin, and we can obtain specific values for a_i and b_i .

$$N_i(h) = \frac{\zeta_0 I_0}{b_i - a_i} \left[-\left(\frac{a_i + b_i}{1!} \right) h + \left(\frac{a_i^2 + b_i^2}{2!} \right) h^2 + \sigma(a_i^2 + b_i^2) \right] \quad (30)$$

a_i		b_i	
7842.83 ± 20.15	3422.01 ± 4.71	3752.31 ± 0.35	4544.01 ± 0.86
6771.29 ± 0.00	8109.61 ± 0.70	352.54 ± 0.02	2743.27 ± 2.89

Figure 15: Specific Values of a_i and b_i

5.3 Task 4 : Atmospheric Delay for Observations with Small

Elevation Angles

As shown in the figure 15, the results are more stable and accurate after adding the ionosphere consideration.

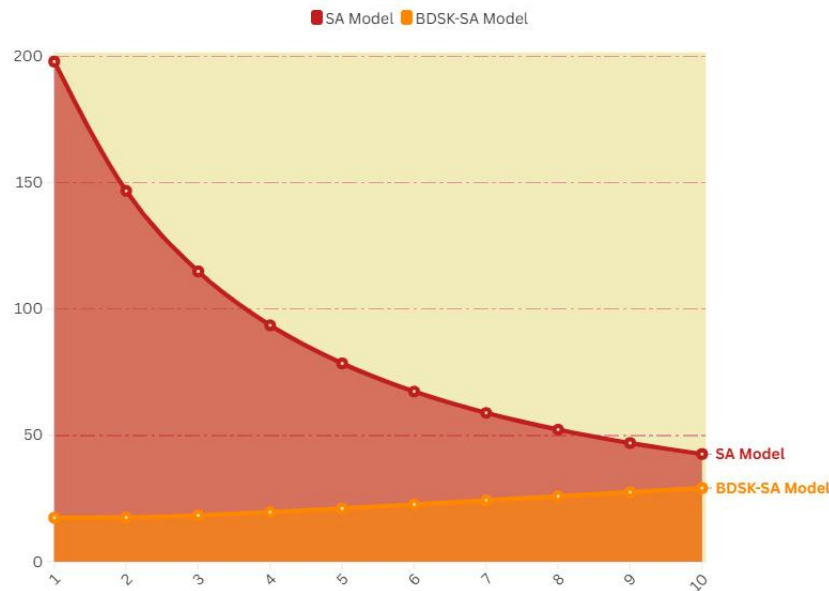


Figure 16: SA Model and BDSK-SA Model

6. Sensitivity Analysis

In the previous articles, we have built TVF-EMD Model, SA Model and BDSK-SA Model for a total of four tasks. In this post, we focus on the stability of the latter two.

In the model for Task 3, the question asked us to find the atmospheric refraction delay of zenith refraction at incident frequencies greater than 20 GHz to be less than or equal to 7.69 ns. Our model should be generalized to all regions at high incident angles. Therefore, we calculate the atmospheric refraction delays at 70°-90° for each of the six regions: Chongqing, Urumqi, Beijing, Nanjing, Hohhot, and Haikou, and plot the corresponding images:

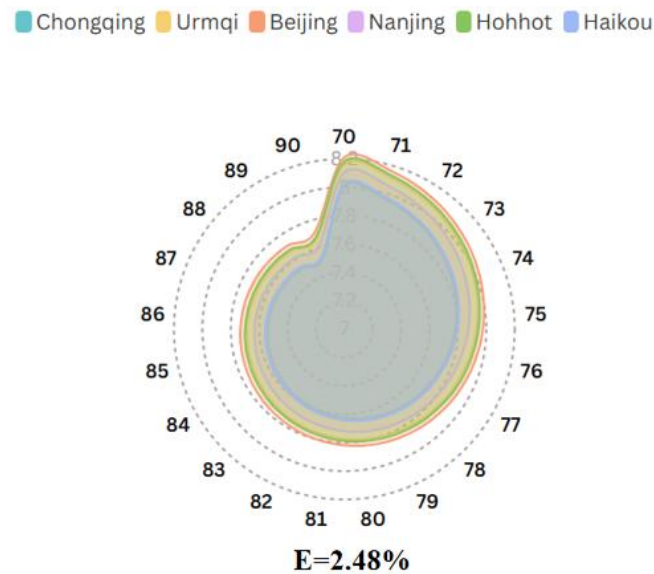


Figure 17: Atmospheric Refraction Delay at High Angles

From the above figure we find that the atmospheric refraction delay fluctuates in the range of 7.5 ns-8.1 ns for all six cities. Some of the results above 7.69 ns are due to the fact that we changed the angle of incidence of the incident light not the zenith delay. None of our data changed with large fluctuations for the different six cities and non-zenith delays. Thus proving the accuracy of our Task 3 SA Model.

In the model of Task 4, we calculate the atmospheric refraction delay for angles of incidence less than 10 and improve the model to increase the accuracy. We analyzed the stability of its latitude, selected 0 degrees to 90 degrees in turn to calculate the corresponding atmospheric refraction delay, and plotted the corresponding stacked diagram:

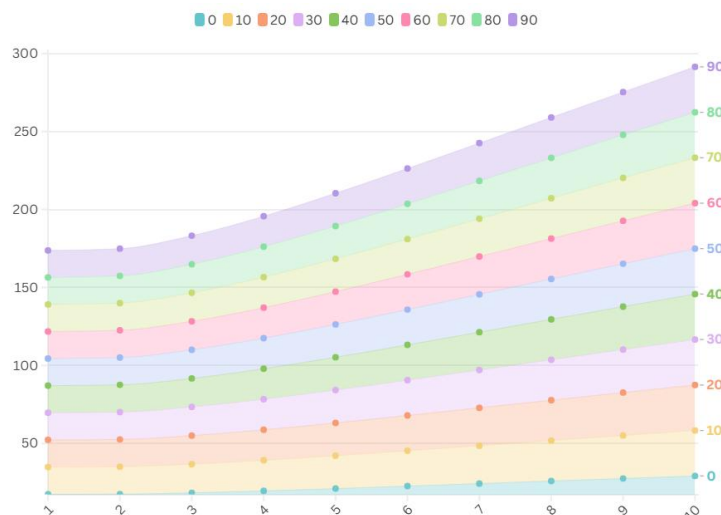


Figure 18: Stacked Map at Low Angles

Similarly, we can find that the atmospheric refraction delays in all six regions fluctuate in the range of about 20 ns and do not differ significantly. Thus proving the

stability of our BDSK-SA Model.

7. Strengths and Weakness

7.1 Strengths

- In the model for Tasks 1 and 2 we fit the timing noise curve as a sine function with five different periods, and then summed them up to fit the whole EMD curve. This separate fitting makes our fitted noise more physically meaningful, takes into account more subtle effects, and is realistic. The final fitted curve has a 98.6% degree of match.
- In the end we get a fitted curve consisting of a combination of five sine functions with different periods. The new formula is simpler and reduces computational stress.
- In the SA model of Task 3 we differentiate the atmospheric water vapor content at different altitudes into static and wet atmospheres, and introduce the concept of mapping function to make the model more generalizable.
- In Task 4, considering the fact that the distance traveled by the pulsed signal becomes longer at small-angle incidence and that the effect of the ionosphere is not negligible, we have taken ionospheric refraction into account, greatly improving the accuracy of our modeled atmospheric refraction delays.

7.2 Weaknesses

- Our final predicted image in Task 2 has a strong periodic overshoot and contains too many small twists and turns in each cycle compared to the actual image that preceded it. It does not match the actual image.
- Our SA model has a low atmospheric refraction delay only at high incidence angles. As the incidence angle increases, the accuracy of the atmospheric refraction delay still produces an unavoidable degradation even with the correction.

8. Conclusion

Pulsar, as the "lighthouse of the universe", its observation and analysis has long been a fascinating subject. This paper not only fits a specific pulsar timing noise, shows the fitting methods and effect of predictions, but also studies the time delay in neutral and ionospheric atmosphere models, preparing for future observations and correction of pulsar signals, and looking forward to uncover more mysteries of the universe through these signals.

References

- [1]Hartnett G.J., and Luiten N.A., Comparison of astrophysical and terrestrial frequency standards, *Review of Modern Physics*, 83(1): 1-9,2011
- [2]Astronomy Now, Researchers find a new way to weigh pulsars, <https://astronomynow.com/2015/10/05/researchers-find-a-new-way-to-weigh-a-pulsar/>, 2024.11.16.
- [3]Sebastian Golat, Carlo R. Contaldi, Geodesic noise and gravitational wave observations by pulsar timing arrays, *Physics Letters B*, 818: 1-5, 2021
- [4]Schnitzeler, D. H. F. M., & Bassa, C. G., A Comprehensive Study of the Influence of the Interstellar Medium on Pulsar Timing and Its Implications for Timing Array Experiments, *Monthly Notices of the Royal Astronomical Society*, 446(4): 3920-3936, 2015
- [5]Gao, F., Gao, Y.P., & Tong, M.L. et al., Application of Analysis and Prediction of Pulsar Timing Residuals Based on the Method of Empirical Mode Decomposition, *Acta Astronomica Sinica*, 59(4): 3-13,2018.
- [6]Dongxing Xu, Jianchuan Yin, An enhanced hybrid scheme for ship roll prediction using support vector regression and TVF-EMD, *Ocean Engineering*, 307: 117951, 2024
- [7]J.R.K. Kumar Dabbakuti, Rangababu Peesapati, Kiran Kumar Anumandla, Algorithm for ionosphere delay computation based on Klobuchar-like coefficients for regional navigation satellite system users, *Advances in Space Research*, 70(10): 2920-2928, 2022
- [8]Ahao Wang, Yize Zhang, Junping Chen, Shijie Li, Zehao Zhang, Hu Wang, Analysis of spatial – temporal characteristics for BDS-3 broadcast ionospheric models (BDS Klobuchar and BDGIM) in multi-GNSS real-time single-frequency precise point positioning, *Measurement*, 224: 113958, 2024
- [9]Anis Allagui, Hachemi Benaoum, Oleg Olendski, On the Gouy – Chapman – Stern model of the electrical double-layer structure with a generalized Boltzmann factor, *Physica A: Statistical Mechanics and its Applications*, 582: 126252, 2021